APPLIED SCIENCES AND ENGINEERING

Welding of 3D-printed carbon nanotube–polymer composites by locally induced microwave heating

Charles B. Sweeney,[1,2] Blake A. Lackey,[1] Martin J. Pospisil,[1] Thomas C. Achee,[1] Victoria K. Hicks,[1] Aaron G. Moran,[1] Blake R. Teipel,[3] Mohammad A. Saed,[4] Micah J. Green[1,2]*

Additive manufacturing through material extrusion, often termed three-dimensional (3D) printing, is a burgeoning method for manufacturing thermoplastic components. However, a key obstacle facing 3D-printed plastic parts in engineering applications is the weak weld between successive filament traces, which often leads to delamination and mechanical failure. This is the chief obstacle to the use of thermoplastic additive manufacturing. We report a novel concept for welding 3D-printed thermoplastic interfaces using intense localized heating of carbon nanotubes (CNTs) by microwave irradiation. The microwave heating of the CNT-polymer composites is a function of CNT percolation, as shown through in situ infrared imaging and simulation. We apply CNT-loaded coatings to a 3D printer filament; after printing, microwave irradiation is shown to improve the weld fracture strength by 275%. These remarkable results open up entirely new design spaces for additive manufacturing and also yield new insight into the coupling between dielectric properties and radio frequency field response for nanomaterial networks.

INTRODUCTION

For typical three-dimensional (3D)–printed parts, the extruded filament traces display tensile properties similar to injection-molded samples in the print (x) direction (Fig. 1A). However, the filament traces are aligned orthogonal to the y and z (build) directions such that tensile properties in these directions are limited by the interfacial bonding strength of the filaments. Thus, despite additive manufacturing's versatility and speed, the mechanical properties of 3D-printed parts currently lag behind those of conventionally manufactured parts. This is one of the principal barriers to widespread adoption of material extrusion (ME) as a means to industrial manufacturing, along with speed and cost (1).

The reason for this limitation is because polymer interfacial diffusion and filament bonding only occur if the polymer is heated above its critical sintering temperature (2–4). Because of the limited time at these high temperatures, conventional ME yields incomplete filament bonding and creation of mechanical failure points. Previous efforts to increase this heating time using heated air nozzles have resulted in morphology disruption, particularly in small samples (5). This creates a critical processing trade-off, where uniform heating warps the structure, but a lack of heating results in poor welds. This processing difficulty prompts a more fundamental scientific question of how the filaments can be thermally bonded without bulk heating and deformation of the structure.

A solution to this problem is to apply heat directly at the polymer interface at a length scale much smaller than the filament trace dimensions, analogous to traditional macroscale metal welding. We posit that the use of nanoscale radio frequency (RF) susceptors, localized at the interface, may provide vigorous, targeted heating. In particular, carbon nanotubes (CNTs) are known to rapidly evolve heat upon exposure to microwave radiation (6–12). This effect occurs for both single- and multi-walled CNTs (SWCNTs and MWCNTs, respectively); other nanomaterials such as graphene nanoribbons have demonstrated similar heating, albeit at far slower heating rates (13, 14). The first report of using CNTs to bond polymer substrates using microwave heating was by Zhang and co-workers (15). Other groups have demonstrated that strong welds may be achieved between thermoplastic interfaces using microwave heating of CNTs (16–18).

We now introduce a new technology called locally induced RF (LIRF) welding that uses MWCNTs' local heating properties to enable additive manufacturing of high-strength materials (patent pending). After thermoplastic filaments are coated with an MWCNT-rich polymer film (Fig. 1A), 3D printing of these filaments results in a macroscopic structure, with MWCNTs localized only at the interfaces between each trace. Upon exposure to microwave irradiation (Fig. 1B), these MWCNT-loaded interfaces selectively heat, which promotes increased local polymer mobility and entanglement across the interface. LIRF technology solves the problem described above by creating interfaces loaded with nanoscale, microwave-responsive heating elements.
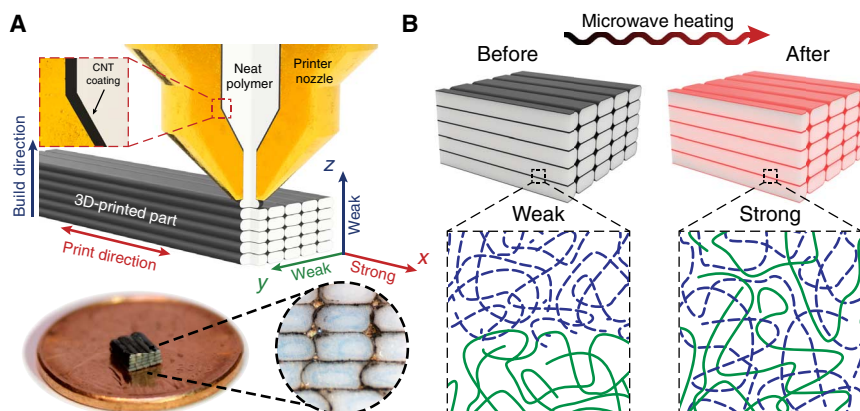
RESULTS

To deploy LIRF technology in a 3D-printed part, a material embodiment new to additive manufacturing is necessary. Our new coaxial filament structure is fabricated by way of a bath coating process (Fig. 2A), wherein a thin coaxial MWCNT ink is applied to the exterior of a feedstock polylactide (PLA) 3D printer filament (Fig. 2B). In addition, we have demonstrated that a similar coated filament structure may be accomplished with a melt extrusion process by coextruding a CNT masterbatch over a neat polymer core, proving that this technology is industrially scalable. We selected an engineering grade of PLA as a model 3D printing polymer, given its balance of strength and stiffness relative to conventional engineering-grade plastics. The low melt temperature allows for processing on standard open-air desktop 3D printers. The ink is made by sonicating MWCNTs in chloroform and shear-mixing with a PLA/chloroform solution. When melt extruded through a standard 3D printer nozzle, the coating remains intact and thins because of extensional flow of the polymer (Figs. 1A and 2C). Optical microscopy shows that the as-printed structure has the desired MWCNT-loaded interfaces (Fig. 2D).

[1]Artie McFerrin Department of Chemical Engineering, Texas A&M University, College Station, TX 77843, USA. [2]Department of Materials Science and Engineering, Texas A&M University, College Station, TX 77843, USA. [3]Essentium Materials LLC, College Station, TX 77845, USA. [4]Department of Electrical and Computer Engineering, Texas Tech University, Lubbock, TX 79409, USA.
*Corresponding author. Email: micah.green@tamu.edu

Fig. 1. (A) 3D-printed parts tend to display weak tensile properties in the y and z directions due to poor interlayer welding. To address this, we coated thermoplastic filament with a CNT-rich layer; the resulting 3D-printed part contains RF-sensitive nanofillers localized at the interface. **(B)** When a microwave field is applied, the interface is locally heated to allow for polymer diffusion and increased fracture strength.
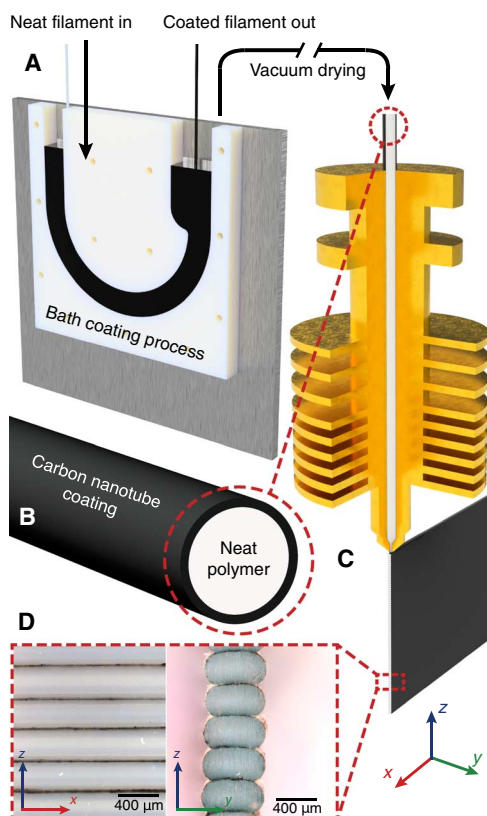

Fig. 2. (A) Thermoplastic filaments are coated with a CNT/polymer ink and dried to create **(B)** coaxial filaments, where only the exterior is RF-sensitive. **(C)** These filaments may be 3D-printed to form structures with CNTs localized at each interface. **(D)** Optical micrographs of sanded cross sections show that CNTs do not migrate into the filament interior during printing.

This technology relies on the precise composition and microwave responsiveness of the coating. The specific MWCNT content in the coating and the relative thickness of the coating must be chosen to allow for microwave heating even after the printing process, which thins the coating considerably. Hence, we examined the properties of homogeneous MWCNT/PLA coatings by hot pressing solution-cast MWCNT/PLA films with MWCNT mass loadings from 0 to 20 weight % (wt %). We then performed AC dielectric measurements and DC conductivity measurements to characterize the percolation behavior of the MWCNT network (Fig. 3A) (19). In addition, we measured the transmitted, reflected, and dissipated power of the films using a two-port coaxial line technique (Fig. 3B). These dielectric measurements are then correlated with thermal imaging during microwave exposure. The hot-pressed films were heated in a rectangular waveguide powered by a solid-state microwave source operated at 2.45 GHz, whereas spatial temperature measurements were carried out using an infrared camera system (Fig. 3, C and D) (20). We observed a strong correlation between electrical percolation and the heating response of the films, with a major increase in the heating rate above the percolation threshold (12). This implies that there is a minimum MWCNT loading in the film to achieve a rapid heating response. Counterintuitively, the heating response then decreases (Fig. 3C) and becomes less uniform at higher MWCNT loadings. This surprising result occurs because, at higher loadings, the films become more reflective and thus less absorptive to incident microwaves (Fig. 3B). This finite range of loading, where there is strong coupling between the electromagnetic field and composite, is necessary for maximizing both heating rate and uniformity. This phenomenon has not been applied to composite processing in previous literature. We also conducted finite-element simulations of microwave adsorption and heat transfer using COMSOL Multiphysics (Fig. 3E); similar trends appear, showing that these concepts can be accurately simulated from first principles. (Details for FLIR measurements, heating rate measurements, and finite element simulations are included in figs. S1 to S7.)

These heating experiments and simulations directly inform the choice of coating composition, the coating thickness, and the microwave parameters used for the actual heating process (discussed in more detail in figs. S8 to S14). Of course, all this characterization is for homogeneous MWCNT-loaded polymer films; to relate this work back to our 3D-printed structures, we both measured and simulated MWCNT-coated filament bundles. Cross sections of coated filaments were super glued to a PLA film to create a bundle (fig. S15). The bundle was then placed in a waveguide and irradiated at 150 W. The temperature was monitored using a FLIR camera equipment with a microscopic lens and FLIR software. It is clear from the FLIR image (fig. S16) that heat emanates from the peripheral circumference of the filaments in the bundle, which coincides directly with the nanotube
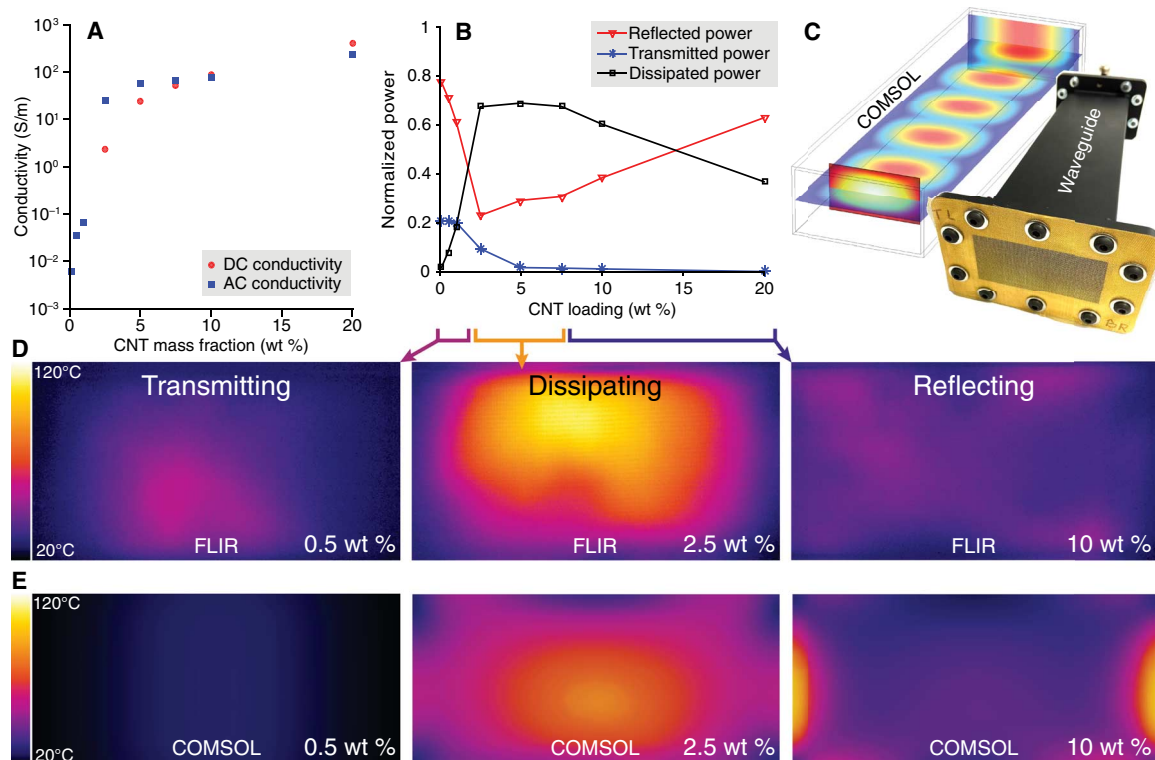
Fig. 3. The dielectric properties and microwave heating response of CNT-loaded PLA films are probed as a function of nanotube loading. (A) Classic percolation behavior is observed for these nanotube networks. **(B)** Percolation is associated with a marked increase in the dissipated power, but at high loadings, the conductive network becomes reflective. **(C)** In situ infrared imaging is used to capture the **(D)** heating response of the nano-filled films, and the same two transitions are observed. This trend is corroborated by **(E)** COMSOL finite-element simulations of RF heating and heat transfer.

coating. This site-specific heat source sets up a thermal gradient between the coating and the interior of the neat PLA filament. We simulated the same bundle geometry in COMSOL with an applied electromagnetic boundary surface heat source at the filament circumference and observed a thermal gradient consistent with the temperature profile observed in the FLIR recording. Additional constraints on the coating composition are imposed by the extrusion process. There is a maximum MWCNT loading in the coating based on the ability of the coating and filament to co-flow during extrusion; at higher loadings, flow instabilities may result. Similarly, the coating thickness is determined by a trade-off between the need to generate heat and the need to localize that heat. For our experiments, we selected a coating containing 10 wt % MWCNTs and a coating thickness of approximately 14 μm.

For the microwave exposure process itself, the underlying polymer physics are an example of classic polymer welding; three critical parameters define the system: time, temperature, and pressure. In an additive manufacturing context, one cannot control pressure, and uniform heating warps the as-printed structure. Therefore, we use the embedded MWCNT coating to control the temperature at the interface for a given time. The CNT composite–coated filament was used to print the coupons used for the microwave heat treatment and mechanical testing. Samples were printed on an ME or fused filament fabrication style 3D printer (Stacker 500) shown in fig. S17. (Details of 3D printing and microwave exposure are given in figs. S17 to S22.) The nozzle bore on the Stacker 500 was fixed at 0.5 mm in diameter (fig. S18). Rectangular sample coupons, a single trace in width, were printed

in the vertical (z) direction in a continuous spiral pattern to ensure that each layer had a spatially uniform thermal history during printing (Fig. 2C). We then exposed the samples to microwaves in our waveguide apparatus, and the temperature was monitored using a FLIR camera as before. From a processing standpoint, it is desirable to minimize the time required to weld the interfaces. Semicrystalline polymers, including PLA, benefit from having the interface above the melting point of the polymer so that crystalline regions can melt, diffuse, and recrystallize across the weld line (21–23). For our microwave heat treatments, we used an exposure time of 60 s at 160°C. Note that these temperatures are too low to induce structural changes or covalent alterations in the MWCNTs (6, 10).

To determine the strengthening effect of the LIRF welding process on 3D-printed interfaces, we selected a mode III tear propagation resistance ("trouser tear") test suitable for thin plastic sheets (ASTM D1938) illustrated in Fig. 4A. This technique was identified as a standard test to gauge the fracture strength of 3D-printed interfaces (24). The sample is torn such that the fracture propagates along a single z direction weld line. This test method accurately gauges the fracture strength of a single 3D-printed layer weld line as it fails via the slip-stick mechanism; this is a mode III analog to a double cantilever beam (mode I) test (25). The results of the trouser tear tests are presented in Fig. 4B for neat hot-pressed films (that is, bulk polymer with no-weld line) and 3D-printed coupons including both neat- and CNT LIRF–welded specimens. (CNT-coated specimens without the LIRF treatment behave similarly to the neat specimen; details of the tests are shown in figs. S23 to S30.)
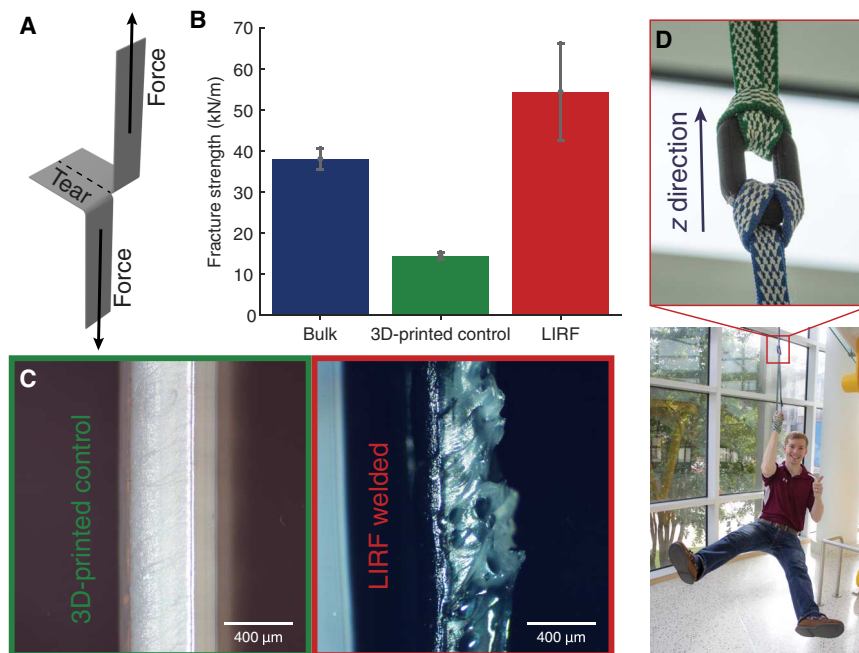
Fig. 4. (A) Tear tests are used to determine that **(B)** the fracture strength of 3D-printed PLA coupons is increased by 275% when CNT coatings and LIRF welding are applied. **(C)** Optical micrographs of the fracture surfaces reveal significant necking and crazing in the LIRF-welded sample, whereas the smooth surface of the 3D-printed control sample indicates a brittle fracture. **(D)** A nanotube-coated, LIRF-welded PLA chain link printed in the z direction is able to support the weight of C.B.S. This LIRF welding enables new, high-strength applications of additive manufacturing.

DISCUSSION

The results of these tests indicate that the LIRF welding process is a highly effective technique for strengthening the interfaces of 3D-printed parts; fracture strength increased by 275% over baseline 3D-printed parts. Both optical microscope and scanning electron microscopy (SEM) images of the fracture surfaces for the three samples (hot-pressed bulk PLA; 3D-printed neat PLA; and CNT-coated, 3D-printed, LIRF-welded PLA) are shown in Fig. 4C and figs. S32 to S42. It is clear that the bulk hot-pressed PLA sample undergoes significant plastic deformation during the propagation of the tear. This plastic deformation and crazing is absent in the neat 3D-printed control sample; instead, a clean and smooth fracture surface can be seen. Minor surface crazing is visible on the neat PLA printed samples at large magnifications; however, the lack of any visible bulk plastic deformation confirms the brittle fracture.

In stark contrast, the fracture surfaces (figs. S34 to S42) of the LIRF-welded samples exhibit large necked zones along the tear path with significant bulk plastic deformation. The fracture surfaces of LIRF-welded samples closely resemble those of the bulk hot-pressed PLA films. This evidence leads us to the conclusion that both the strength and ductility of the samples have been restored. The fracture strength results support this conclusion; in some of the LIRF-welded samples, the propagation of the crack along the weld line was pinned such that the crack deviated from the center line and tore diagonally or perpendicularly to the weld line. (This tendency is commonly seen in tear tests as noted in ASTM D1938 sec. 9.4.) The LIRF-welded parts outperform even the neat hot-pressed films; this suggests that the heat treatment may locally increase the crystallinity of the polymer interface or that the MWCNTs reinforce the interface after the welding process.

We highlight another important observation about the structure of the samples after the LIRF heat treatment. In the SEM images (figs. S40 to S42), one can clearly observe that the printed layers have not been structurally altered or warped after the welding has occurred. This proves that the localized heating process is capable of increasing the interlayer bond strength without sacrificing the dimensional accuracy of the part.

These enhancements in 3D-printed weld strength imply that MWCNT coatings on polymer filaments, followed by LIRF heating, can allow for 3D-printed structures with properties approaching those of conventional manufacturing. This enables load-supporting structures with complex shapes such as the 3D-printed chain link shown in Fig. 4D. In our upcoming studies, we anticipate that this process can be extended to additive manufacturing of other thermoplastics; other electromagnetic frequencies may also be feasible for LIRF welding. Furthermore, these results indicate that conventional bulk heating of polymers to induce welding could be replaced by localized RF-responsive coatings.

MATERIALS AND METHODS

CNTs were first sonicated in 50 ml of chloroform for 30 min, whereas the PLA was dissolved in 50 ml of chloroform. The solid content of each solution was held constant at 4 mg/ml, whereas the CNT wt % was varied. Solutions were produced in a 0.5, 1.0, 2.5, 5.0, 7.5, 10, and 20 wt % CNTs. After sonication, CNTs were mixed with the dissolved PLA and placed in a glass petri dish. The petri dish was left in a fume hood overnight to let most of the chloroform evaporate off. The next day, the CNT/PLA film was placed in the vacuum oven for 24 hours to remove the remaining chloroform. After vacuum drying, the films were then removed from the petri dish.

The vacuum-dried cast films were then compacted and pressed with a parallel plate hot press (Carver 3856) at 150°C and 27.6 MPa. Two machined steel shims 0.5 mm in thickness were placed on either side of the films to maintain a constant thickness between all samples.

Trouser tear test samples were tested according to ASTM D1938 standards on an Instron 5944 mechanical tester (figs. S23 and S24) fitted with a 500-N load cell and equipped with Bluehill software. Samples were tested at a strain rate of 100 mm/min. The thickness of the fracture surface was calculated from end-view fracture surface images as shown in fig. S25; the mean value for 3D-printed samples was found to be 0.419 mm. The thickness for the bulk PLA hot press films was measured for each sample using a micrometer as specified by ASTM D1938. Samples were loaded into the Instron grips and pulled until the tear had propagated along the entire sample length. Load versus extension was recorded in the Instron Bluehill software. These plots were converted to fracture strength versus extension plots to normalize for the thickness of the sample. The fracture strength was calculated using the following formula

$$S_F = \frac{2F_N}{t}$$

where S_F is the fracture strength, F_N is the normal force, and t is the thickness of the sample as determined above.

Fracture strength plots for all the samples including the bulk hot-pressed PLA, printed neat and CNT control samples, and the printed LIRF-welded samples are shown below (figs. S26 to S30). To determine the average fracture strength value along the weld line, it is necessary to disregard the initial and final portions of the force (fracture strength) versus extension curve as specified by ASTM D1938 standards. We used MATLAB to select the first peak in the data during the linear loading of the sample tabs. This automatically selects the first slip-stick criteria as the neat film or weld line begins to fracture. The start point in the data is indicated by a triangle on each plot. For the end of test criteria, the minimum force value before the onset of tensile crazing (hardening) was determined, and data 1 mm before this point were truncated. The truncated final portions of the curve are plotted in gray. The data in between these points were averaged to determine the mean fracture strength of each tear.

In addition, we conducted a short study analyzing the effect of nozzle temperature on the fracture strength of the neat PLA printed coupons (fig. S31). This was inspired by similar tests conducted at the National Institute of Standards and Technology. (24) We did this to ensure that we used the "best-case" settings for the 3D-printed baseline samples. Nozzle temperatures from 200° to 240°C were selected on the basis of the lowest temperature possible for printing the material, up to the highest temperature (240°C) where degradation of the PLA is expected to occur. As can be observed in the plots, the higher temperatures resulted in consistently stronger welds; this influenced our decision to print the control samples at the highest nozzle temperature setting of 240°C. Note that we did not use any nozzle air cooling from the fan for similar reasons; air cooling was found to reduce the fracture strength of the weld line.

SUPPLEMENTARY MATERIALS

CNT/PLA hot-pressed films and electrical characterization
Microwave heating thermometry for hot-pressed films
COMSOL
Heating response as a function of thickness
Microwave bonding of thermoplastic interfaces
Filament coating method
Heating response of coated filaments
3D printing ASTM D1938 tear test coupons
Microwave exposure of tensile coupons
Mode III fracture strength (trouser tear) testing method
Mode III fracture strength (trouser tear) testing results
table S1. DC conductivity measurement details.
table S2. Material properties used in COMSOL calculations.
table S3. Material properties of PLA filament.
fig. S1. Dielectric measurements using a sample holder placed between two coaxial transmission lines.
fig. S2. AC dielectric properties including the real part of the relative permittivity, the loss tangent, and AC conductivity.
fig. S3. FLIR thermal image screenshots of hot-pressed PLA films after 30 s of heating at 15 W.
fig. S4. Max temperature versus time for various wt % of CNTs in waveguide, 15-W microwave power.
fig. S5. Geometry used in COMSOL simulations.
fig. S6. Differential scanning calorimetry data for PLA.
fig. S7. COMSOL simulation predictions for temperature (average) versus time for all samples.
fig. S8. Setup for spray coating PLA films outlined in the "COMSOL" section.
fig. S9. The microwave response of 10 wt % MWCNT spray-coated PLA films (as quantified by the mean temperature of the film at 30 s) versus film thickness.
fig. S10. Stress versus strain for lap-shear samples.
fig. S11. Coating bath internal view.
fig. S12. Microscope image of the 1.75-mm printer filament with CNT coating.
fig. S13. Microscope image of the coated filament after being extruded from a 0.5-mm nozzle.
fig. S14. Schematic for calculation of coating thickness.
fig. S15. Coated PLA filament array glued to polymer film.
fig. S16. FLIR image of coated filament bundle heating in waveguide and corresponding COMSOL simulation of filament bundle heating in a waveguide.
fig. S17. Stacker 500 desktop 3D printer.
fig. S18. Stacker printer nozzle showing heat sink.
fig. S19. Slicing pattern and G-code preview of the rectangular tear specimens.
fig. S20. FLIR camera positioned over the waveguide to directly measure sample temperature during exposure to microwaves.
fig. S21. Microwave choke tube designed to attenuate and contain microwave energy yet still allow for direct viewing of sample.
fig. S22. Maximum temperature versus time for all five LIRF samples.
fig. S23. Instron 5944 load frame used for tensile and tear tests.
fig. S24. Close-up view of sample gripped in the tensile load frame.
fig. S25. Optical microscope image of a tear test sample viewed edge-on to determine the mean weld line thickness.
fig. S26. Tear test fracture strength versus extension results for bulk PLA film.
fig. S27. Tear test fracture strength versus extension results for neat printed PLA.
fig. S28. Tear test fracture strength versus extension results for CNT-coated printed PLA.
fig. S29. Tear test fracture strength versus extension results for CNT-coated, LIRF-welded printed PLA samples.
fig. S30. Tear test fracture strength results for each sample type.
fig. S31. Tear test fracture strength versus extension results for nozzle temperature sweep.
fig. S32. Optical microscope image of tear test fracture surface for bulk hot-pressed PLA sample (necking and crazing are clearly visible).
fig. S33 Optical microscope image of tear test fracture surface for neat 3D-printed PLA control sample (necking and crazing are absent; instead, a clean fracture surface is observed).
fig. S34 Optical microscope image of tear test fracture surface for LIRF-welded sample (necking and crazing are clearly visible).
fig. S35. Optical microscope image of tear test fracture surface for LIRF-welded sample (necking and crazing are clearly visible).
fig. S36. SEM image of tear test fracture surface for neat PLA 3D-printed tear samples.
fig. S37. SEM image of tear test fracture surface for neat PLA 3D-printed tear samples.
fig. S38. SEM image of tear test fracture surface for neat PLA 3D-printed tear samples.
fig. S39. SEM image of tear test fracture surface for neat PLA 3D-printed tear samples.
fig. S40. SEM image of tear test fracture surface for LIRF-welded, 3D-printed PLA tear test samples (necking and crazing are clearly visible).
fig. S41. SEM image of tear test fracture surface for LIRF-welded, 3D-printed PLA tear tests.
fig. S42. SEM image of tear test fracture surface for LIRF-welded, 3D-printed PLA tear test samples (necking and crazing are clearly visible).

REFERENCES AND NOTES

1. O. Ivanova, C. Williams, T. Campbell, Additive manufacturing (AM) and nanotechnology: Promises and challenges. *Rapid Prototyping J.* **19**, 353–364 (2013).
2. Q. Sun, G. M. Rizvi, C. T. Bellehumeur, P. Gu, Experimental study of the cooling characteristics of polymer filaments in FDM and impact on the mesostructures and

properties of prototypes, *Proceedings of the 14th Solid Freeform Fabrication Symposium*, Austin, TX, 4 to 6 August 2003.

3. C. Bellehumeur, L. Li, Q. Sun, P. Gu, Modeling of bond formation between polymer filaments in the fused deposition modeling process. *J. Manuf. Process.* **6**, 170–178 (2004).

4. Q. Sun, G. M. Rizvi, C. T. Bellehumeur, P. Gu, Effect of processing conditions on the bonding quality of FDM polymer filaments. *Rapid Prototyping J.* **14**, 72–80 (2008).

5. S. C. Partain, *Fused Deposition Modeling with Localized Pre-Deposition Heating Using Forced Air* (Montana State University, 2007).

6. E. Vázquez, M. Prato, Carbon nanotubes and microwaves: Interactions, responses, and applications. *ACS Nano* **3**, 3819–3824 (2009).

7. R. H. Baughman, A. A. Zakhidov, W. A. de Heer, Carbon nanotubes—The route toward applications. *Science* **297**, 787–792 (2002).

8. V. K. Rangari, M. S. Bhuyan, S. Jeelani, Microwave processing and characterization of EPON 862/CNT nanocomposites. *Mater. Sci. Eng.* **168**, 117–121 (2010).

9. F. G. Brunetti, M. A. Herrero, J. d. M. Muñoz, A. Díaz-Ortiz, J. Alfonsi, M. Meneghetti, M. Prato, E. Vázquez, Microwave-induced multiple functionalization of carbon nanotubes. *J. Am. Chem. Soc.* **130**, 8094–8100 (2008).

10. T. J. Imholt, C. A. Dyke, B. Hasslacher, J. M. Perez, D. W. Price, J. A. Roberts, J. B. Scott, A. Wadhawan, Z. Ye, J. M. Tour, Nanotubes in microwave fields: Light emission, intense heat, outgassing, and reconstruction. *Chem. Mater.* **15**, 3969–3970 (2003).

11. A. Mashal, B. Sitharaman, X. Li, P. K. Avti, A. V. Sahakian, J. H. Booske, S. C. Hagness, Toward carbon-nanotube-based theranostic agents for microwave detection and treatment of breast cancer: Enhanced dielectric and heating response of tissue-mimicking materials. *IEEE Trans. Biomed. Eng.* **57**, 1831–1834 (2010).

12. K. R. Paton, A. H. Windle, Efficient microwave energy absorption by carbon nanotubes. *Carbon* **46**, 1935–1941 (2008).

13. H. C. Shim, J.-W. Song, Y. K. Kwak, S. Kim, C.-S. Han, Preferential elimination of metallic single-walled carbon nanotubes using microwave irradiation. *Nanotechnology* **20**, 065707 (2009).

14. N. D. Kim, A. Metzger, V. Hejazi, Y. Li, A. Kovalchuk, S.-K. Lee, R. Ye, J. A. Mann, C. Kittrell, R. Shahsavari, J. M. Tour, Microwave heating of functionalized graphene nanoribbons in thermoset polymers for wellbore reinforcement. *ACS Appl. Mater. Interfaces* **8**, 12985–12991 (2016).

15. M. Zhang, S. Fang, A. A. Zakhidov, S. B. Lee, A. E. Aliev, C. D. Williams, K. R. Atkinson, R. H. Baughman, Strong, transparent, multifunctional, carbon nanotube sheets. *Science* **309**, 1215–1219 (2005).

16. C. Y. Wang, T. G. Chen, S. C. Chang, S. Y. Cheng, T. S. Chin, Strong carbon-nanotube–polymer bonding by microwave irradiation. *Adv. Funct. Mater.* **17**, 1979–1983 (2007).

17. T. Wu, Y. Pan, E. Liu, L. Li, Carbon nanotube/polypropylene composite particles for microwave welding. *J. Appl. Polym. Sci.* **126**, E283–E289 (2012).

18. S. Poyraz, L. Zhang, A. Schroder, X. Zhang, Ultrafast microwave welding/reinforcing approach at the interface of thermoplastic materials. *ACS Appl. Mater. Interfaces* **7**, 22469–22477 (2015).

19. M. A. Saed, A method of moments solution of a cylindrical cavity placed between two coaxial transmission lines. *IEEE Trans. Microw. Theory Tech.* **39**, 1712–1717 (1991).

20. E. Vargas, M. L. Pantoya, M. A. Saed, B. L. Weeks, Advanced susceptors for microwave heating of energetic materials. *Mater. Des.* **90**, 47–53 (2016).

21. T. Ge, G. S. Grest, M. O. Robbins, Tensile fracture of welded polymer interfaces: Miscibility, entanglements, and crazing. *Macromolecules* **47**, 6982–6989 (2014).

22. J. Vogel, M. R. Kessler, S. Sundararajan, D. Grewell, Activation energy for diffusion and welding of PLA films. *Polym. Eng. Sci.* **52**, 1693–1700 (2012).

23. H. Zhang, D. Fortin, H. Xia, Y. Zhao, Fast optical healing of crystalline polymers enabled by gold nanoparticles. *Macromol. Rapid Commun.* **34**, 1742–1746 (2013).

24. J. E. Seppala, in *SPE ANTEC* (Indianapolis, 2016).

25. V. Kishore, C. Ajinjeru, A. Nycz, B. Post, J. Lindahl, V. Kunc, C. Duty, Infrared preheating to improve interlayer strength of big area additive manufacturing (BAAM) components. *Addit. Manuf.* **14**, 7–12 (2017).